

High-voltage output triboelectric nanogenerator with DC/AC optimal combination method

Yuqi Wang^{1,2,§}, Tian Huang^{1,§}, Qi Gao^{1,§}, Jianping Li³, Jianming Wen³ (✉), Zhong Lin Wang^{1,4,5} (✉), and Tinghai Cheng^{1,2,4} (✉)

¹ Beijing Institute of Nanoenergy and Nanosystems, Chinese Academy of Sciences, Beijing 101400, China

² School of Mechatronic Engineering, Changchun University of Technology, Changchun 130012, China

³ The Institute of Precision Machinery and Smart Structure, Key Laboratory of Intelligent Operation and Maintenance Technology & Equipment for Urban Rail Transit of Zhejiang Province, College of Engineering, Zhejiang Normal University, Jinhua 321004, China

⁴ CUSTech Institute of Technology, Wenzhou 325024, China

⁵ School of Materials Science and Engineering, Georgia Institute of Technology, Atlanta, GA 30332-0245, USA

[§] Yuqi Wang, Tian Huang, and Qi Gao contributed equally to this work.

© Tsinghua University Press and Springer-Verlag GmbH Germany, part of Springer Nature 2021

Received: 19 September 2021 / Revised: 25 October 2021 / Accepted: 25 October 2021

ABSTRACT

The high-voltage power source is one of the important research directions of triboelectric nanogenerator (TENG). In this paper, a high-voltage output TENG (HVO-TENG) is proposed with direct current/alternating current (DC/AC) optimal combination method for wind energy harvesting. Through the optimal design of a direct current generation unit (DCGU) and an alternating current generation unit (ACGU), the HVO-TENG can produce DC voltage of 21.5 kV and AC voltage of 200 V, simultaneously. The HVO-TENG can continuously illuminate more than 6,000 light emitting diodes (LEDs), which is enough to drive more possible applications of TENG. Besides, this paper explored application experiments on HVO-TENG. Demonstrative experiments indicate that the high-voltage DC output is used for producing ozone, while the AC output can light up ultraviolet (UV) LEDs. The HVO-TENG can increase the ozone concentration (C) in an airtight container to 3 parts per million (ppm) after 7 h and continuously light up UV LEDs. All these demonstrations verify that the HVO-TENG has important guiding significance for designing high performance TENG.

KEYWORDS

triboelectric nanogenerator, high voltage, direct current/alternating current (DC/AC) optimal combination, wind energy harvesting

1 Introduction

High-voltage power sources are widely used in human life, such as agricultural insecticides [1] and electrostatic generators [2]. The current method of producing high-voltage power usually requires a complex power converter, which greatly increases the complexity and cost of the system [3]. Moreover, the portability and safety of the traditional high-voltage power source are also issues needed to be solved [4]. By contrast, triboelectric nanogenerator (TENG) has the inherent characteristics of high voltage and low current, which makes TENG unprecedented portability and safety [5].

TENG with high-voltage characteristics first was proposed by Wang's group in 2012 [6], which can convert mechanical energy extensively existing in the environments into electric energy [7–10]. As a new energy harvesting technology, TENG has the characteristics of easy fabrication, low cost, and multitudinous choices of structures [11–13], which is widely concerned by researchers [14–17]. Based on these advantages, TENG has been widely used in many fields [18–21], such as intelligent transportation [22, 23], environmental protection [24, 25],

harvesting environmental energy [26–28], harvesting blue energy [29–31], and oil purification [32], negative air ion generator [33], plasma applications [34], and disinfection [35–37]. Besides, to further broaden the application of TENG, studying high performance strategies for TENG is necessary.

Herein, a high-voltage output triboelectric nanogenerator (HVO-TENG) is proposed with direct current/alternating current (DC/AC) optimal combination method. It consists of two generation units: a direct current generation unit (DCGU) and an alternating current generation unit (ACGU). Through the optimized design of the generation units, the length (L) of the aluminum electrode, the central angle (θ_1) of the aluminum electrode, and the central angle (θ_2) of the fluorinated ethylene propylene (FEP) films are finally determined, achieving maximum output performance of the HVO-TENG. Theoretical calculation results show that DCGU can generate a high voltage of 21.5 kV, and experiments show that the ACGU can generate a voltage of 200 V, simultaneously. In addition, more than 6,000 light emitting diodes (LEDs) can continuously be lighted up using the HVO-TENG, which indicates a higher output capacity. Besides, the HVO-TENG can generate ozone and ultraviolet (UV) at the same

Address correspondence to Jianming Wen, wjming@zjnu.cn; Zhong Lin Wang, zhong.wang@mse.gatech.edu; Tinghai Cheng, chengtinghai@binn.cas.cn

time, by combining the corona discharge and UV LEDs into DCGU and ACGU. The HVO-TENG can increase the ozone concentration (C) in a 12 L airtight container to 3 parts per million (ppm), after 7 h of operation, and UV LEDs can be light continuously. In general, HVO-TENG can be used as a high-voltage power source, and it has great prospect for applying TENG in the field of environmental energy harvesting in the future.

2 Results and discussion

2.1 Structure design and operation mechanism

The basic structure of the HVO-TENG is demonstrated in Fig. 1. The HVO-TENG is comprised of a wind scoop, a driving unit, generation units, and an output module (Fig. 1(a)(i)). The mechanism of the driving unit is shown in Fig. 1(a)(ii). The input shaft connected to the wind scoop drives the chucks through gears, and the generation units are installed on the chucks. Therefore, when the wind scoop is blown, rotor-A and rotor-B in the generation units will rotate with the chucks (Fig. S1 in the Electronic Supplementary Material (ESM)). Besides, the generation units contain a DCGU and an ACGU (Fig. 1(a)(iii)). As the two sets of gears have the same transmission ratios and different numbers of idler wheels, the rotation directions of the rotors are different, and the speeds are the same. To better harvest wind energy, the gear is designed to reduce the start-up wind speed of HVO-TENG. When the transmission ratio is 0.5, the starting wind speed of HVO-TENG is $4.53 \text{ m}\cdot\text{s}^{-1}$ (gentle breeze), which happens to be a common wind speed in natural environments. To better describe the structure of the prototype, Fig. 1(b) shows the overall structure of the HVO-TENG, and Figs. 1(c)(i) and 1(c)(ii) illustrate the shapes of the stators and rotors in the generation units.

Figure 2(a)(i) illustrates the composition of the generation units. The conductive rod-1 outputs DC, while the conductive rod-2 is responsible for transferring the charge of the DCGU. In the ACGU, the FEP films are fixed on both rotor-A and rotor-B and

sweep stator-A and stator-B (Fig. 2(a)(ii)). The operation mechanism of the DCGU is depicted in Fig. 2(b). As the FEP films rub the aluminum electrodes (Fig. 2(b)(i)), the aluminum electrodes at each end of the conductive rod-2 have opposite charges. When rotor-A rotates, the aluminum electrodes will be charged with equal amounts of positive or negative charges. Then the positive and negative charges will respectively output through the conductive rod-1 (Fig. 2(b)(ii)). The same variation occurs on rotor-B (Figs. 2(b)(iii) and 2(b)(iv)). The functions of FEP and nylon films are to maximize the charge on rotor-A and rotor-B.

The operation mechanism of the ACGU is depicted in Fig. 2(c). The copper-1 and copper-2 have connected alternately through the external circuit. When the FEP films in the ACGU are in the initial position, the copper-1 and the FEP films will respectively induce equal amounts of opposite charges (Fig. 2(c)(i)). With the running of the FEP films, the FEP films come into contact with copper-2 (Fig. 2(c)(ii)). The positive charges are transferred from copper-1 to the copper-2 through the external circuit due to electrostatic induction. When the FEP films are totally in contact with copper-2, all positive charges will flow to copper-2 (Fig. 2(c)(iii)). After the FEP films separate from copper-2, another operation cycle begins and hence the AC is generated. Furthermore, to prove the feasibility of the prototype, 2-dimensional simulation results got from COMSOL Multiphysics 5.2a software clarify the operation mechanism of the HVO-TENG (Fig. S2 in the ESM).

2.2 Output performance

To realize the better performance of the HVO-TENG, the generation units were optimized. First, a system experiment was carried out to explore the performance of the DCGU. The L of the aluminum electrode in the DCGU was researched (Fig. 3) when the stepper motor was 270 rpm. When the L is 60 or 90 mm, the open-circuit voltage (V_{OC}), short-circuit current (I_{SC}) and transferred charge (Q_{SC}) are shown in Figs. 3(a) and 3(b), and each set of illustrations includes the shape of the aluminum electrode and the signal of the magnified view. Herein, two parameters, the

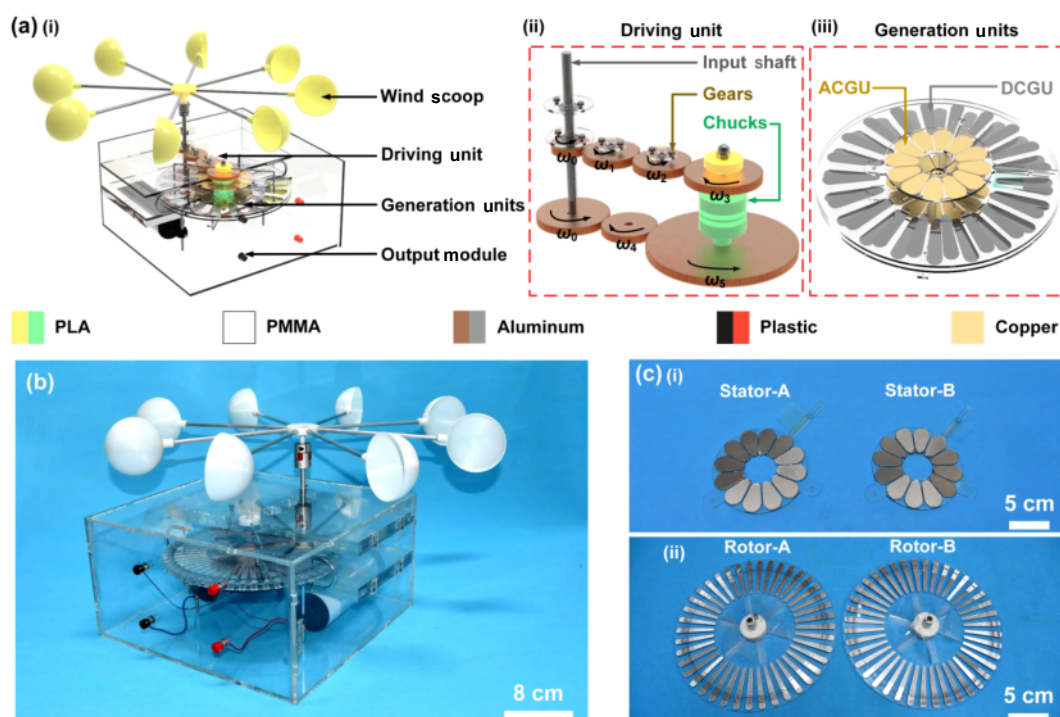


Figure 1 3-dimensional model of HVO-TENG. (a) The 3-dimensional structure diagram includes overall structure (i), driving unit (ii), generation units (iii) of the HVO-TENG. (b) and (c) Actual pictures of (b) entire device, and (c) stators (i), and rotors (ii) in the generation units.

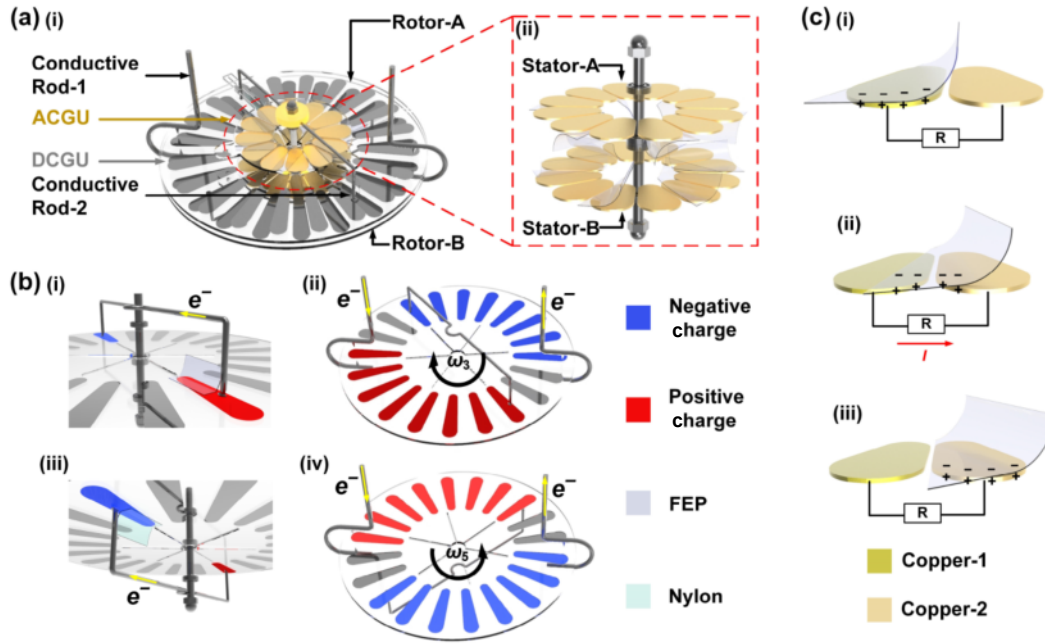


Figure 2 (a) Structures of generating units. (b) and (c) Mechanisms of the transferred charge of DCGU (b) and ACGU (c).

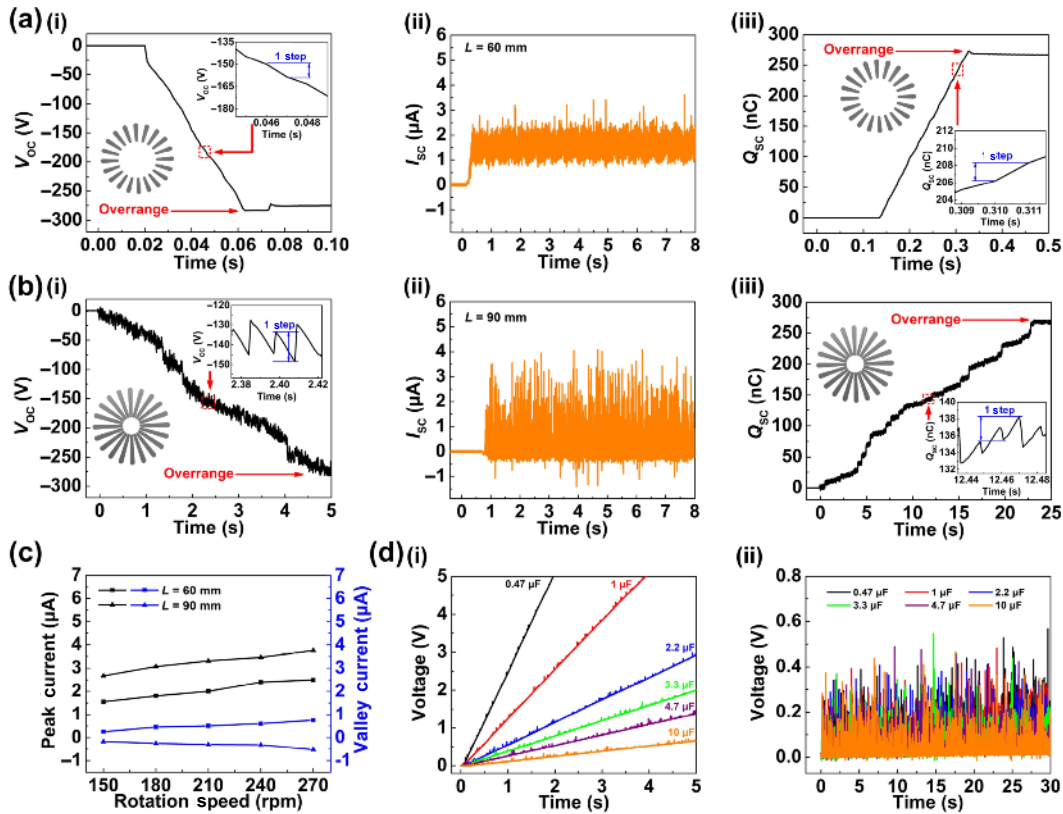


Figure 3 (a) and (b) The performance of DCGU with the L of the aluminum electrode 60 mm (a) and 90 mm (b). (c) The relationship between rotation speed and I_{SC} . (d) The charging curve under different capacitance values by DCGU with L of 60 mm (i) and 90 mm (ii).

peak value and valley value of current, were used to reveal the performance I_{SC} (Fig. 3(c)). As the speed of the stepper motor increases from 150 to 270 rpm, the peak value of I_{SC} with L of 60 mm increases slowly from 1.6 to 2.5 μA , and the valley value of current increases from 0.3 to 0.8 μA , indicating the enhanced charge replenishment from transporting-electrodes to accumulators. For the case of 90 mm, the peak value of I_{SC} increases slowly from 2.7 to 3.7 μA , while the valley value decreases from -0.2 to -0.5 μA , which is adverse. It can be speculated that the aluminum electrodes in the central area of rotor-A and rotor-B always overlap when the L is 90 mm, which

affects the performance of DCGU. Under no bridge rectifier in this experiment, the voltage signals of different capacitors charged when L is 60 and 90 mm, respectively (Figs. 3(d)(i) and 3(d)(ii)). A capacitor of 0.47 μF can be charged to 5.0 V within 1.9 s, revealing that the output capacity of the DCGU is better when the L is 60 mm.

Then the influence of the θ_1 of the aluminum electrode in the DCGU on the output performance was explored (Fig. 4). When the speed of the stepper motor is 270 rpm with θ_1 of 4° , the V_{OC} and Q_{SC} are shown in Figs. 4(a) and 4(b), and the dependence of the voltage, current of the DCGU on external resistance is given in

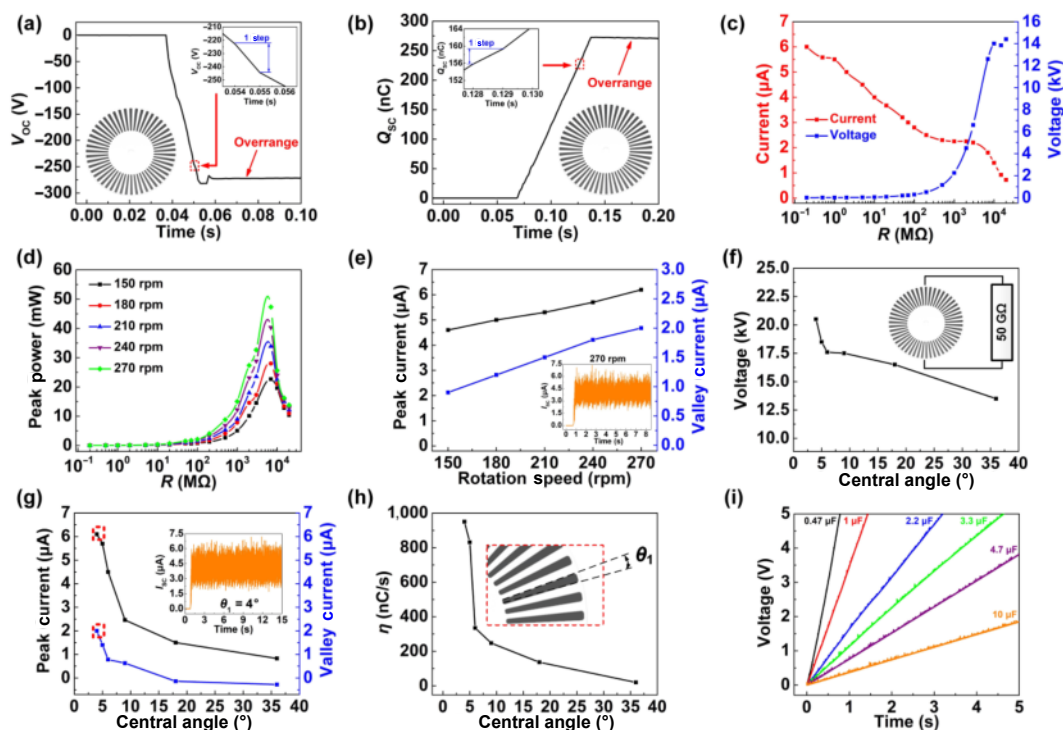


Figure 4 The output performance of the DCGU: V_{OC} (a); Q_{SC} (b). (c) The dependence of the output current, voltage on different resistive loads. (d) The relationship between different rotation speeds and dependence of peak power on different resistive loads. (e) and (f) The relationship between rotation speed and I_{SC} (e), and θ_1 of the aluminum electrode and V_{OC} (f). (g) and (h) The relationship between θ_1 and I_{SC} (g), and θ_1 and speed rate (h) of transferred charge. (i) The charging curves under different capacitance values by DCGU when the θ_1 is 4° .

Fig. 4(c). The relationships of the peak power of the DCGU on external resistance at different rotation speeds are given in Fig. 4(d), and the maximum peak power of the DCGU can reach 47.3 mW. A sample of the DCGU I_{SC} is shown in Fig. 4(e), where the peak and valley values of the current are used to reveal the performance I_{SC} . When the speed increases from 150 to 270 rpm, the peak and valley values of the I_{SC} increase from 4.6 to 6.2 and 0.9 to 2.0 μA , respectively, indicating that the charge supplementation from the aluminum electrode to the battery is enhanced. In addition, the relationship between rotation speed and Q_{SC} is shown in Fig. S3 in the ESM.

Since the V_{OC} exceeded the range of the programmable electrometer, a 50 G Ω resistor was added to calculate the output voltage of the DCGU [32]. The calculated output voltage gradually increases as the θ_1 becomes smaller, and the maximum value is 21.5 kV (Fig. 4(f)). As the θ_1 increases from 4° to 36° , the peak value and the valley value of I_{SC} gradually decrease from 6.1 and 2.0 to 0.8 and -0.3 μA (Fig. 4(g)), which shows the weakening of DCGU. Because the charge will accumulate at the edge or tip of the metal, the smaller the θ_1 is, the greater the charge density is on the surface of the aluminum foil; finally, the smaller the θ_1 is, the greater the I_{SC} is, which can be explained by Eq. S1 in the ESM. The original data of I_{SC} are shown in Fig. S4 in the ESM. To further clarify the effect of θ_1 on DCGU performance, the speed rate of accumulation charge (η) is shown in Eq. S2 in the ESM. Therefore, when L is 60 mm and θ_1 is 4° , the output performance of the DCGU is the maximum (Fig. 4(h)). This DCGU was used to charge different commercial capacitors without a bridge rectifier (Fig. 4(i)). In conclusion, this fully confirms the output capability of HVO-TENG.

Because the central region of the rotor is unused when L is 60 mm, the ACGU is installed in the middle blank area of rotor-A and rotor-B to improve the utilization of the generation units. The insets in Fig. 5 reveal the influence of FEP film parameters and stepper motor rotation speed on the ACGU output performance.

The corresponding V_{OC} , I_{SC} , and Q_{SC} of the different θ_2 of the FEP films with 150 rpm are shown in Figs. 5(a)–5(c). The detail of the θ_2 is shown in Fig. S5 in the ESM. The ACGU reaches its maximum output performance when θ_2 is 55° : The V_{OC} , I_{SC} , and Q_{SC} are respectively 200 V, 2.5 μA , and 75 nC. When the speed of stepper motor is increased from 150 to 270 rpm with other conditions remaining constant, the V_{OC} , I_{SC} , Q_{SC} are shown in Figs. 5(d)–5(f). When the rotation speed is 270 rpm, the dependence of the voltage, current of the ACGU on external resistance is given in Fig. 5(g). The peak powers of the ACGU at different rotation speeds on external resistance are shown in Fig. 5(h), and the maximum peak power is 0.9 mW. Figure 5(i) Figure 5(i) reveals the charging curves under different capacitance values by ACGU.

2.3 Demonstration

To verify the application ability of HVO-TENG, a series of experiments are presented in Fig. 6. Parameters L , θ_1 , and θ_2 in HVO-TENG are set to 60 mm, 4° , and 55° , respectively. The HVO-TENG can light up more than 6,000 LEDs, which proves the high-voltage output capability of the HVO-TENG (Fig. 6(a) and Movie S1 in the ESM). Meanwhile, Fig. 6(b) shows the experimental system of the HVO-TENG for ozone and UV production. The metal rod-1 (MR-1), metal rod-2 (MR-2), and UV LED board are loaded in a 12 L airtight container made of acrylic. The MR-1 and MR-2 are connected to the DCGU through capacitors, and the UV LED board is connected to the ACGU through a bridge rectifier. When the wind scoop is blown about 4.53 $\text{m}\cdot\text{s}^{-1}$, the HVO-TENG starts to operate. The MR-1 and MR-2 can create corona discharges as the DCGU continuously charges the capacitor, while the UV LED board can be lit up by the ACGU (Fig. 6(c) and Movie S2 in the ESM), and both of them will produce ozone. An ozone detector detects the gradual increase of the C inside the airtight container. Figure 6(d) depicts the variation of C in a 12 L airtight container within 24 h operation of

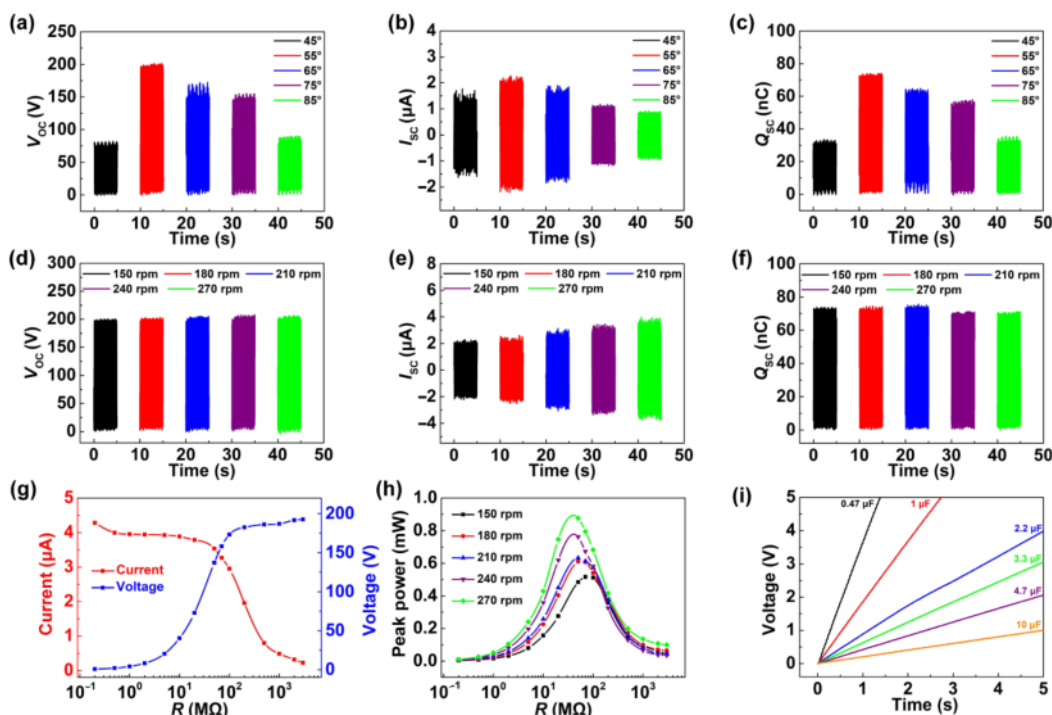


Figure 5 Output performance of the ACGU: (a) and (d) V_{OC} ; (b) and (e) I_{SC} ; (c) and (f) Q_{SC} . (g) The dependence of the output current, voltage on different resistive loads. (h) The relationship between rotation speed and peak power of the ACGU. (i) Figure 5(i) reveals the charging curves under different capacitance values by ACGU.

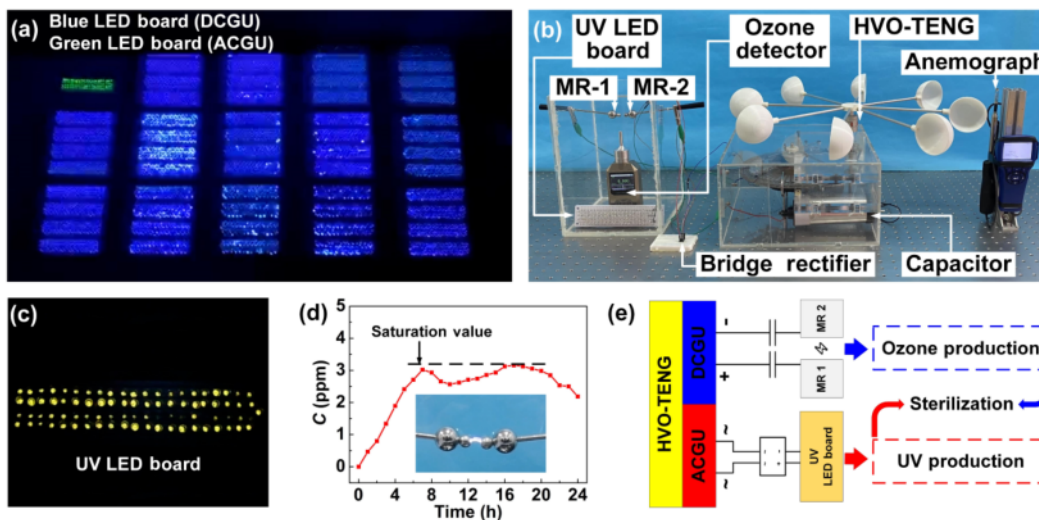


Figure 6 (a)–(c) Application demonstration of HVO-TENG. (d) The relationship between the time and C in the airtight container. (e) A proposed sterilization system based on the HVO-TENG.

HVO-TENG. The detected ozone is formed by converting the oxygen in the airtight container through corona discharge. Therefore, with the continuous ionization of the air by HVO-TENG, the ozone concentration in the airtight container increases gradually. However, because the container is airtight, the rate of ozone production decreases with the decrease of oxygen concentration. In addition, because ozone is unstable in the air, ozone is also decomposing during the experiments. Therefore, the ozone concentration will fluctuate near the saturation value after a period of time.

In addition, this article proposes a sterilization system based on the HVO-TENG (Fig. 6(e)). Chen et al. have confirmed the feasibility of combined ozone and UV sterilization [38], and this article also tested the antibacterial properties of HVO-TENG [39, 40]. The detailed experimental procedures are shown in Table S1 in the ESM.

3 Conclusions

In summary, this article proposes an HVO-TENG with DC/AC optimal combination method for wind energy harvesting. Both the DCGU and the ACGU are optimal designed and installed in the generation units. Besides, the effects of the aluminum electrode and FEP films in the generation units on the output of the HVO-TENG are studied and the optimal parameters assembly is obtained. The HVO-TENG can output 21.5 kV DC voltage and 200 V AC voltage. Finally, the HVO-TENG combines with the corona discharge generated by DCGU and UV LEDs lighted by ACGU, establishing a self-powered ozone and UV generation system for sterilization. Experiments show that the HVO-TENG can increase the C in a 12 L airtight container, which reaches 3 ppm after 7 h and continuously light up a UV LED board. The proposed HVO-TENG, as an ultrahigh-voltage power source, can realize the high-voltage DC output simultaneously with additional

AC output. It has guiding significance for investigating high performance TENGs.

4 Experimental section

4.1 Fabrication of the HVO-TENG

The HVO-TENG had a dimension of 576 mm (length) × 576 mm (width) × 297 mm (height). The frame of HVO-TENG was made of a laser-cutting acrylic plate and a 3-dimensional printing polylactic acid (PLA). The driving unit of the HVO-TENG was machined by a lathe. The thickness of FEP films, aluminum electrodes, and copper electrodes were 100, 100 and 65 μm, respectively. Other information is given in the ESM.

4.2 Electrical measurement

The rotation was generated by a stepper motor (J-5718HBS401, Yisheng, China), and the signal of the HVO-TENG was captured by a programmable electrometer (6514, Keithley, USA) and a data acquisition card (USB-6218, National Instruments, USA). The signal was transmitted to the computer and recorded by LabVIEW. The ozone concentration was captured by an ozone detector (PLT300-O³, Pulitong, China).

Acknowledgments

The authors are grateful for the support received from the National Key R&D Project from the Minister of Science and Technology (Nos. 2016YFA0202701 and 2016YFA0202704), the Beijing Municipal Science and Technology Commission (No. Z171100002017017).

References

- [1] Huang, K.; Li, K. L.; Shu, L.; Yang, X.; Gordon, T.; Wang, X. C. High voltage discharge exhibits severe effect on ZigBee-based device in solar insecticidal lamps internet of things. *IEEE Wirel. Commun.* **2020**, *27*, 140–145.
- [2] Dobrowolski, A.; Pieloth, D.; Wiggers, H.; Thommes, M. Electrostatic precipitation of submicron particles in a molten carrier. *Pharmaceutics* **2019**, *11*, 276.
- [3] Wu, C. S.; Wang, A. C.; Ding, W. B.; Guo, H. Y.; Wang, Z. L. Triboelectric nanogenerator: A foundation of the energy for the new era. *Adv. Energy Mater.* **2019**, *9*, 1802906.
- [4] Wang, Z. L.; Wang, A. C. On the origin of contact-electrification. *Mater. Today* **2019**, *30*, 34–51.
- [5] Wang, Z. L. Triboelectric nanogenerator (TENG)-sparking an energy and sensor revolution. *Adv. Energy Mater.* **2020**, *10*, 2000137.
- [6] Fan, F. R.; Tian, Z. Q.; Wang, Z. L. Flexible triboelectric generator. *Nano Energy* **2012**, *1*, 328–334.
- [7] Zhong, J. W.; Zhong, Q. Z.; Fan, F. R.; Zhang, Y.; Wang, S. H.; Hu, B.; Wang, Z. L.; Zhou, J. Finger typing driven triboelectric nanogenerator and its use for instantaneously lighting up LEDs. *Nano Energy* **2013**, *2*, 491–497.
- [8] Tang, Q.; Yeh, M. H.; Liu, G. L.; Li, S. M.; Chen, J.; Bai, Y.; Feng, L.; Lai, M. H.; Ho, K. C.; Guo, H. Y. et al. Whirligig-inspired triboelectric nanogenerator with ultrahigh specific output as reliable portable instant power supply for personal health monitoring devices. *Nano Energy* **2018**, *47*, 74–80.
- [9] Wang, P. H.; Pan, L.; Wang, J. Y.; Xu, M. Y.; Dai, G. Z.; Zou, H. Y.; Dong, K.; Wang, Z. L. An ultra-low-friction triboelectric-electromagnetic hybrid nanogenerator for rotation energy harvesting and self-powered wind speed sensor. *ACS Nano* **2018**, *12*, 9433–9440.
- [10] Tcho, I. W.; Jeon, S. B.; Park, S. J.; Kim, W. G.; Jin, I. K.; Han, J. K.; Kim, D.; Choi, Y. K. Disk-based triboelectric nanogenerator operated by rotational force converted from linear force by a gear system. *Nano Energy* **2018**, *50*, 489–496.
- [11] Wang, Z. L.; Zhu, G.; Yang, Y.; Wang, S. H.; Pan, C. F. Progress in nanogenerators for portable electronics. *Mater. Today* **2012**, *15*, 532–543.
- [12] Wang, Z. L. Triboelectric nanogenerators as new energy technology for self-powered systems and as active mechanical and chemical sensors. *ACS Nano* **2013**, *7*, 9533–9557.
- [13] Das, P. S.; Chhetry, A.; Maharjan, P.; Rasel, M. S.; Park, J. Y. A laser ablated graphene-based flexible self-powered pressure sensor for human gestures and finger pulse monitoring. *Nano Res.* **2019**, *12*, 1789–1795.
- [14] Wang, Z. L. Triboelectric nanogenerators as new energy technology and self-powered sensors—principles, problems and perspectives. *Faraday Discuss.* **2014**, *176*, 447–458.
- [15] Wang, Z. L.; Jiang, T.; Xu, L. Toward the blue energy dream by triboelectric nanogenerator networks. *Nano Energy* **2017**, *39*, 9–23.
- [16] Wang, Z. L. Entropy theory of distributed energy for internet of things. *Nano Energy* **2019**, *58*, 669–672.
- [17] Liu, L.; Shi, Q. F.; Lee, C. A hybridized electromagnetic-triboelectric nanogenerator designed for scavenging biomechanical energy in human balance control. *Nano Res.* **2021**, *14*, 4227–4235.
- [18] Luo, J. J.; Gao, W. C.; Wang, Z. L. The triboelectric nanogenerator as an Innovative technology toward Intelligent sports. *Adv. Mater.* **2021**, *33*, 2004178.
- [19] Lin, Z. M.; Zhang, B. B.; Guo, H. Y.; Wu, Z. Y.; Zou, H. Y.; Yang, J.; Wang, Z. L. Super-robust and frequency-multiplied triboelectric nanogenerator for efficient harvesting water and wind energy. *Nano Energy* **2019**, *64*, 103908.
- [20] Yang, X. D.; Xu, L.; Lin, P.; Zhong, W.; Bai, Y.; Luo, J. J.; Chen, J.; Wang, Z. L. Macroscopic self-assembly network of encapsulated high-performance triboelectric nanogenerators for water wave energy harvesting. *Nano Energy* **2019**, *60*, 404–412.
- [21] Wang, Z. L. On Maxwell's displacement current for energy and sensors: The origin of nanogenerators. *Mater. Today* **2017**, *20*, 74–82.
- [22] Xu, Y. H.; Yang, W. X.; Yu, X.; Li, H. C.; Cheng, T. H.; Lu, X. H.; Wang, Z. L. Real-time monitoring system of automobile driver status and intelligent fatigue warning based on triboelectric nanogenerator. *ACS Nano* **2021**, *15*, 7271–7278.
- [23] Wang, Y.; Wang, J. Y.; Xiao, X.; Wang, S. Y.; Kien, P. T.; Dong, J. L.; Mi, J. C.; Pan, X. X.; Wang, H. F.; Xu, M. Y. Multi-functional wind barrier based on triboelectric nanogenerator for power generation, self-powered wind speed sensing and highly efficient windshield. *Nano Energy* **2020**, *73*, 104736.
- [24] Han, K.; Luo, J. J.; Feng, Y. W.; Lai, Q. S.; Bai, Y.; Tang, W.; Wang, Z. L. Wind-driven radial-engine-shaped triboelectric nanogenerators for self-powered absorption and degradation of NO_x. *ACS Nano* **2020**, *14*, 2751–2759.
- [25] Leung, S. F.; Fu, H. C.; Zhang, M. L.; Hassan, A. H.; Jiang, T.; Salama, K. N.; Wang, Z. L.; He, J. H. Blue energy fuels: Converting ocean wave energy to carbon-based liquid fuels via CO₂ reduction. *Energy Environ. Sci.* **2020**, *13*, 1300–1308.
- [26] Wang, Y. Q.; Yu, X.; Yin, M. F.; Wang, J. L.; Gao, Q.; Yu, Y.; Cheng, T. H.; Wang, Z. L. Gravity triboelectric nanogenerator for the steady harvesting of natural wind energy. *Nano Energy* **2021**, *82*, 105740.
- [27] Liu, S. M.; Li, X.; Wang, Y. Q.; Yang, Y. F.; Meng, L. X.; Cheng, T. H.; Wang, Z. L. Magnetic switch structured triboelectric nanogenerator for continuous and regular harvesting of wind energy. *Nano Energy* **2021**, *83*, 105851.
- [28] Yang, Y. F.; Yu, X.; Meng, L. X.; Li, X.; Xu, Y. H.; Cheng, T. H.; Liu, S. M.; Wang, Z. L. Triboelectric nanogenerator with double rocker structure design for ultra-low-frequency wave full-stroke energy harvesting. *Extreme Mech. Lett.* **2021**, *46*, 101338.
- [29] Liang, X.; Jiang, T.; Liu, G. X.; Feng, Y. W.; Zhang, C.; Wang, Z. L. Spherical triboelectric nanogenerator integrated with power management module for harvesting multidirectional water wave energy. *Energy Environ. Sci.* **2020**, *13*, 277–285.
- [30] Xia, K. Q.; Fu, J. M.; Xu, Z. W. Multiple-frequency high-output triboelectric nanogenerator based on a water balloon for all-weather water wave energy harvesting. *Adv. Energy Mater.* **2020**, *10*, 2000426.

- [31] Yin, M. F.; Lu, X. H.; Qiao, G. D.; Xu, Y. H.; Wang, Y. Q.; Cheng, T. H.; Wang, Z. L. Mechanical regulation triboelectric nanogenerator with controllable output performance for random energy harvesting. *Adv. Energy Mater.* **2020**, *10*, 2000627.
- [32] Lei, R.; Shi, Y. X.; Ding, Y. F.; Nie, J. H.; Li, S. Y.; Wang, F.; Zhai, H.; Chen, X. Y.; Wang, Z. L. Sustainable high-voltage source based on triboelectric nanogenerator with a charge accumulation strategy. *Energy Environ. Sci.* **2020**, *13*, 2178–2190.
- [33] Guo, H. Y.; Chen, J.; Wang, L. F.; Wang, A. C.; Li, Y. F.; An, C. H.; He, J. H.; Hu, C. G.; Hsiao, V. K. S.; Wang, Z. L. A highly efficient triboelectric negative air ion generator. *Nat. Sustain.* **2021**, *4*, 147–153.
- [34] Cheng, J.; Ding, W. B.; Zi, Y. L.; Lu, Y. J.; Ji, L. H.; Liu, F.; Wu, C. S.; Wang, Z. L. Triboelectric microplasma powered by mechanical stimuli. *Nat. Commun.* **2018**, *9*, 3733.
- [35] Wang, Z. Z.; Shi, Y. X.; Liu, F.; Wang, H.; Liu, X.; Sun, R. T.; Lu, Y. J.; Ji, L. H.; Wang, Z. L.; Cheng, J. Distributed mobile ultraviolet light sources driven by ambient mechanical stimuli. *Nano Energy* **2020**, *74*, 104910.
- [36] Luo, J. J.; Han, K.; Wu, X. Q.; Cai, H. H.; Jiang, T.; Zhou, H. B.; Wang, Z. L. Self-powered mobile sterilization and infection control system. *Nano Energy* **2021**, *88*, 106313.
- [37] Huo, Z. Y.; Kim, Y. J.; Suh, I. Y.; Lee, D. M.; Lee, J. H.; Du, Y.; Wang, S.; Yoon, H. J.; Kim, S. W. Triboelectrification induced self-powered microbial disinfection using nanowire-enhanced localized electric field. *Nat. Commun.* **2021**, *12*, 3693.
- [38] Chen, X. X.; Liu, B.; Chen, Q.; Liu, Y. X.; Duan, X. C. Application of combining ozone and UV-C sterilizations in the artificial drying of persimmon fruits. *LWT* **2020**, *134*, 110205.
- [39] Feng, H. Q.; Bai, Y.; Qiao, L.; Li, Z.; Wang, E. G.; Chao, S. Y.; Qu, X. C.; Cao, Y.; Liu, Z.; Han, X. et al. An ultra-simple charge supplementary strategy for high performance rotary triboelectric nanogenerators. *Small* **2021**, *17*, 2101430.
- [40] Cho, S.; Hanif, Z.; Yun, Y.; Khan, Z. A.; Jang, S.; Ra, Y.; Lin, Z. H.; La, M.; Park, S. J.; Choi, D. Triboelectrification-driven microbial inactivation in a conductive cellulose filter for affordable, portable, and efficient water sterilization. *Nano Energy* **2021**, *88*, 106228.